Development of an Earth SmallSat Flight Test to Demonstrate Viability of Mars Aerocapture

AE 8900 MS Special Problems Report
Space Systems Design Laboratory (SSDL)
Guggenheim School of Aerospace Engineering
Georgia Institute of Technology
Atlanta, GA, 30332

Author:
Michael S. Werner

Advisor:
Robert D. Braun

May 1, 2017

Development of an Earth Smallsat Flight Test to Demonstrate Viability of Mars Aerocapture

Michael S. Werner[1] and Robert D. Braun[2]
Space Systems Design Laboratory, Georgia Institute of Technology, Atlanta, GA, 30318

A smallsat mission concept is developed to demonstrate the feasibility of an aerocapture system at Earth. The proposed mission utilizes aerocapture to transfer from a GTO rideshare trajectory to a LEO. Single-event drag modulation is used as a simple means of achieving the control required during the maneuver. Low- and high-fidelity guidance algorithm choices are considered. Numeric trajectory simulations and Monte Carlo uncertainty analyses are performed to show the robustness of the system to day-of-flight environments and uncertainties. Similar investigations are performed at Mars to show the relevance of the proposed mission concept to potential future applications. The spacecraft design consists of a 24.9 kg vehicle with an attached rigid drag skirt, and features commercially-available hardware to enable flight system construction at a university scale. Results indicate that the proposed design is capable of targeting the desired final orbit, surviving the aerothermodynamic and deceleration environments produced during aerocapture, and downlinking relevant data following the maneuver.

Nomenclature

A	=	aerodynamic reference area
C_D	=	drag coefficient
g_1, g_2	=	deceleration curve-fit accelerometer measurements
m	=	mass
t_{go}	=	time until jettison
β	=	ballistic coefficient
ΔV	=	change in velocity
σ	=	standard deviation

I. Introduction

FUTURE space exploration missions will require the delivery of increasingly massive payloads to different planetary targets. As payload mass continues to increase and more challenging destinations are selected, innovative methods of orbital insertion will be required. For missions to planets with an appreciable atmosphere, aeroassist technologies are promising alternatives to traditional methods. These technologies involve the use of atmospheric forces as a means of deceleration, which may result in mass and cost savings when compared to propulsive insertion.

---

[1] Graduate Research Assistant, School of Aerospace Engineering, 270 Ferst Drive.
[2] David and Andrew Lewis Professor of Space Technology, School of Aerospace Engineering, 270 Ferst Drive.

One such technology is aerocapture. Aerocapture is an orbital maneuver that utilizes the drag generated during atmospheric entry to capture directly into a specific orbit, as shown in Fig. 1. Aerocapture has long been recognized as a technology with a number of potential benefits for space missions[1]. The use of atmospheric drag as a means of deceleration drastically reduces the fuel requirements of many orbital missions, and the single atmospheric pass required for aerocapture can offer reductions in mission time and cost when compared to aerobraking. As a result, aerocapture can improve the size of payloads delivered to specific orbits, and enable other orbits altogether[2].
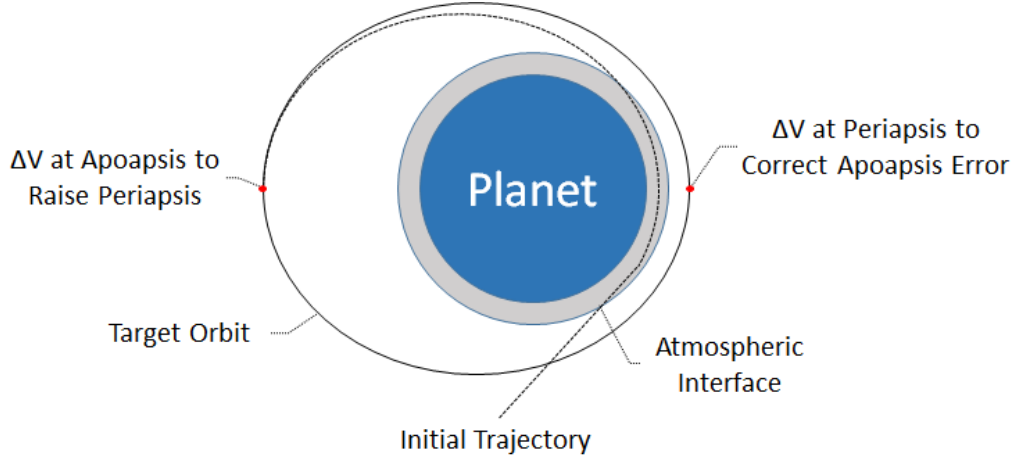

Figure 1. Sample aerocapture mission structure.

Numerous methods of aerocapture have been analytically shown as viable for a range of planetary missions[3-5]. Despite this and the potential benefits of utilizing aerocapture, the technique has not yet been used on a flight mission, with the lack of an integrated flight system demonstration often cited as a rationale. To this end, different flight tests and missions featuring aerocapture have been proposed in the past, although these proposals have been unsuccessful[6]. Simplifying different aspects of the aerocapture mission might yield a flight test that is more likely to be selected by virtue of being less expensive and easier to implement.

Recent research has focused on drag modulation as a means of simplifying traditionally complex control requirements. Drag modulation systems utilize changes in a vehicle's drag area, $C_D A$, during flight to effect control over the vehicle's β and therefore its energy depletion rate and final trajectory:

$$\beta = \frac{m}{C_D A} \tag{1}$$

When compared to traditional bank-to-steer lifting methods, drag modulation techniques enable the use of modest avionics algorithms, sensors, and actuators, and eliminate the need for center-of-gravity offset and an onboard propulsive reaction control system. As a result, drag modulation is a promising technique for facilitating simplistic aerocapture mission architectures.

The most basic form of drag modulation flight control for aerocapture is a single-stage jettison system. An example of this type of system shown in Fig. 2. At atmospheric interface, the vehicle is flying with a large drag device attached, increasing its drag area and thereby lowering its β to β_1. Within the atmosphere, once enough energy has been dissipated to achieve the target orbit, the drag device is jettisoned, increasing the spacecraft's β to β_2. Because of this increase, the vehicle experiences greatly reduced deceleration through atmospheric egress.
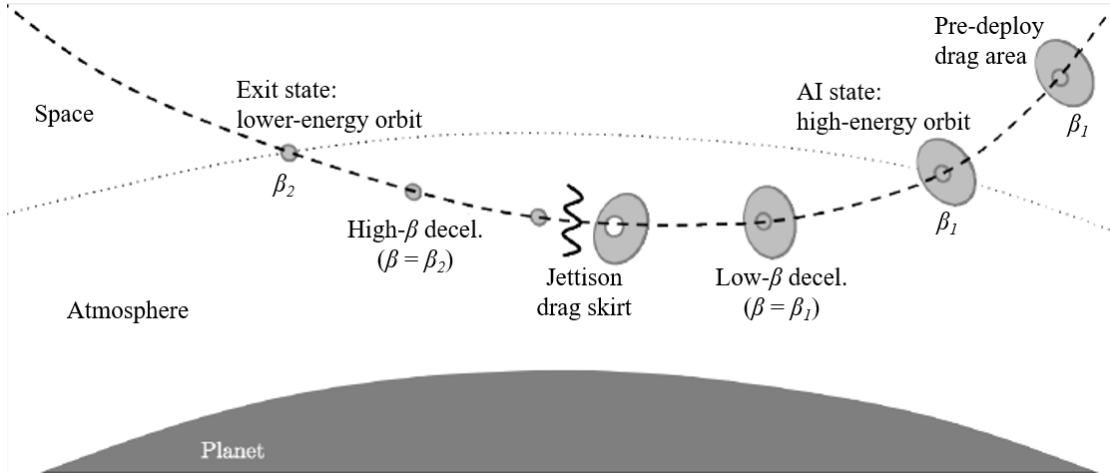
Figure 2. Single-event drag modulation diagram[10].

Drag modulation systems have been paired with aeroassist mission concepts before. McRonald examined the use of trailing inflatable ballutes for planetary entry applications at Mars, Venus, Earth, Titan, and other targets; he noted that releasing the ballute at the appropriate point in an atmospheric trajectory can result in an entry corridor for aerocapture[7]. Jettisoning an attached drag device in this manner accomplishes a single, discrete-event drag modulation, in which a vehicle's β is modified at one discrete point during its trajectory. Other studies have investigated the validity of similar aerocapture mission profiles featuring ballutes[3, 8]. Recently, Putnam et al. examined the performance of continuous and discrete-event drag modulation systems for aerocapture at different celestial targets. For missions to Mars, Titan, and Earth, they showed the existence of feasible entry corridors that are robust to day-of-flight uncertainties[9, 10].

This work is focused on the development of a comprehensive smallsat mission concept that will demonstrate the feasibility of a drag-modulated aerocapture system at Earth. A successful mission would be a simple and inexpensive way to show that drag modulation-based aerocapture can be used as an effective means of orbit insertion at Earth, Mars, and other atmospheric worlds, with scalable applications to both small and large spacecraft. In particular, this investigation is focused on the trajectory design and atmospheric entry analyses of the proposed mission concept. Section 2 describes the proposed mission timeline and success criteria, and presents a nominal spacecraft design. Section 3 outlines the methodology used to analyze the proposed trajectory and to select a guidance scheme. Section 4 showcases the results of an end-to-end mission uncertainty analysis. Section 5 highlights the relevance of the proposed flight test to missions at Mars.

II. Mission and Spacecraft Design

A. Mission Design

The main objective for this mission is to successfully perform an aerocapture maneuver in order to effect a significant change in the spacecraft's orbit. The prevalence of smallsat and CubeSat missions in recent years have shown that minimalistic designs can deliver quality results at a scale conducive to university teams; this type of philosophy was prioritized during mission design.

Specific, high-level mission goals include receiving a nominal ΔV of 2 km/s from a drag-modulated aerocapture maneuver, performing a propulsive maneuver to raise the perigee of the resulting orbit out of Earth's atmosphere, and returning data such that the performance of the aerocapture maneuver can be characterized post-hoc. The specific data products returned are tied to detailed success criteria, shown below in Table 1.

4

Table 1. Mission success criteria.

Success Category	Criteria
Threshold mission success	Spacecraft detected within acceptable range of target final orbit
Baseline mission success	1hz 6-DOF inertial measurement unit (IMU) and thermal data from aerocapture and propulsive maneuvers returned by spacecraft
Bonus mission success	Higher rate IMU and thermal data from aerocapture and propulsive maneuvers returned by spacecraft

The baseline architecture for this mission drew inspiration from the Aerocapture Flight Test Experiment, a prior flight test proposal outlined by Hall in Ref. 6. A timeline of the selected architecture is shown in Fig. 3. Aerocapture normally involves transfer from a hyperbolic orbit to an elliptical orbit around a planetary target. To demonstrate a roughly analogous transfer at Earth, a geosynchronous transfer orbit (GTO) was selected as the spacecraft's high energy initial orbit. Due to the prevalence of communication satellite launches to GTO, this starting orbit enables the smallsat to fly as a secondary payload, which greatly reduces cost when compared to a demonstration requiring a dedicated launch vehicle.
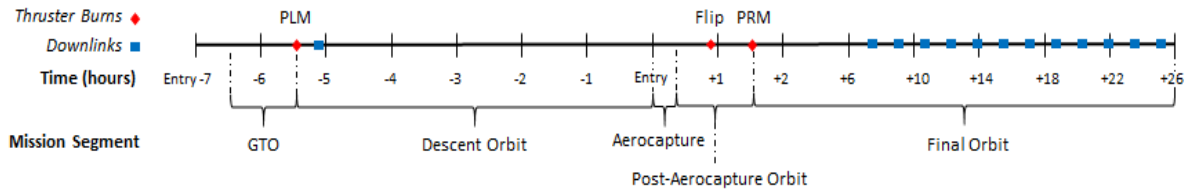

Figure 3. Nominal mission timeline.

The GTO selected for this demonstration has an apogee altitude of 35,786 km and a perigee altitude of 185 km. During the rideshare phase, the host spacecraft will provide power and updated attitude knowledge to the smallsat. It is also desirable that the smallsat be mounted to the host in such a way that an initial spin rate can be imparted before separation, to provide spin stabilization throughout the smallsat's trajectory. Means of achieving this initial spin rate will require further investigation. Separation from the host will occur one hour prior to apogee.

Once the smallsat reaches GTO apogee, it will perform a small propulsive maneuver to lower its perigee into Earth's atmosphere. This perigee-lower maneuver (PLM) is a byproduct of transferring from one elliptical orbit to another, and is not normally required for aerocapture. The PLM will use a predefined amount of fuel to generate a ΔV of 13.2 m/s and will result in a nominal altitude at perigee of 60 km. Following the maneuver, a data downlink will then occur to relay information about the vehicle's health and current orbit. From here, the spacecraft will coast for approximately 5 hours until it reaches Earth's atmosphere.

Following atmospheric interface, single-event drag modulation flight control will be employed to target the desired post-maneuver orbit. The spacecraft will enter the atmosphere traveling approximately 10.3 km/s, with a β that has been lowered via an attached rigid drag skirt. During atmospheric flight, accelerometer data will be used by the flight computer to determine when to jettison the drag skirt such that the target orbit is achieved. After a successful jettison, the smallsat will then exit the atmosphere traveling approximately 8.3 km/s, resulting in an orbit with an apogee altitude of 1,760 km and a perigee altitude of 60 km.

Following atmospheric exit, the spacecraft will utilize the attitude control capabilities of its thrusters to rotate 180 degrees, reorienting its propulsion system for a second burn. Upon reaching apogee of the post-atmospheric orbit approximately 30 minutes after this reorientation, a second propulsive maneuver will be performed to raise the spacecraft's perigee out of Earth's atmosphere. This perigee-raise maneuver (PRM) will require a ΔV of 33.8 m/s and will result in a final orbit with an apogee altitude of 1,760 km and a perigee altitude of 180 km. Once this orbit has been reached, data downlink will begin. The spacecraft will then be left to naturally deorbit within the 25-year timeframe specified by international orbit disposal guidelines.

5

B. Spacecraft Design

The initial mechanical design selected for this mission is shown in Fig. 4, with key aeroshell dimensions listed in Table 2. A 60° sphere-cone form factor was selected due to the benefits it offers for heating, drag, and stability[13], and its use on prior small probe mission such as Genesis[14] and Stardust[15]. As shown in Fig. 4-c, the attached rigid drag skirt was broken into four quadrants, to minimize machining constraints and help reduce the risk of re-impact after jettison. These quadrants are attached to the vehicle via NASA Standard Initiator M3 break bolts, which have been used on a number of prior missions. Both the outer and inner radii of the drag skirt were sized with the goal of maximizing the β-ratio between pre- and post-jettison configurations. As a result, the outer radius matches the largest possible dimension of a typical rideshare constraint, with the inner radius driven by backshell size. Each component of the aeroshell and drag skirt is made of 3mm thick 6061 aluminum to facilitate prototyping and machining at a university scale. A detailed description of the analyses behind the aeroshell design is provided in Refs. 17 and 18.
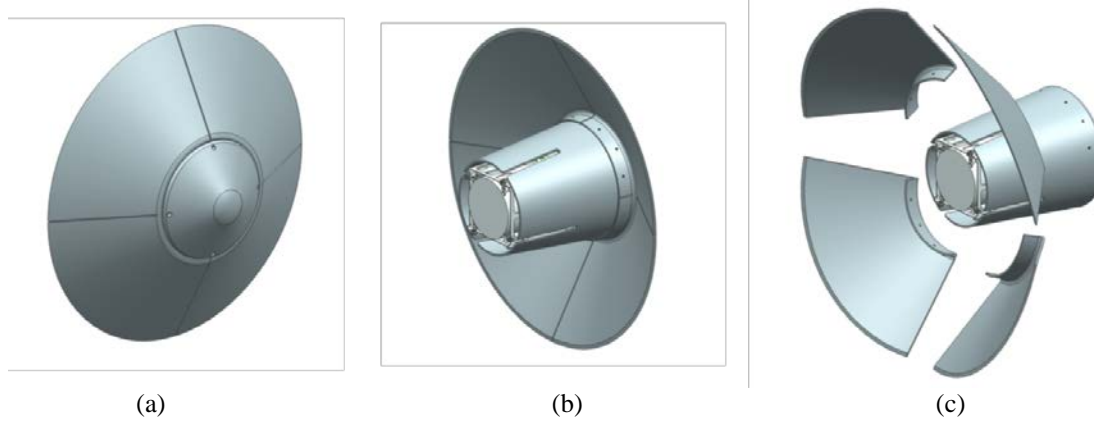

| (a) | (b) | (c) |

Figure 4. Aeroshell CAD views: (a) front isometric, (b) rear isometric, and (c) post-jettison rear isometric.

Table 2. Vehicle design parameters.

Aeroshell Section	Parameter	Value
Foreshell	Radius	10 cm
	Nose radius	5.63 cm
	Shoulder radius	0.56 cm
	Longitudinal length	4.15 cm
	Sphere-cone half angle	60°
	Material thickness	0.3 cm
	Mass	0.27 kg
Backshell	Fore-end radius	10 cm
	Aft-end radius	7.5 cm
	Longitudinal length	21 cm
	Taper angle	5.3°
	Material thickness	0.3 cm
	Mass	0.91 kg
Drag skirt	Outer radius	25 cm
	Inner radius	10 cm
	Sphere-cone half angle	60°
	Material thickness	0.3 cm
	Mass	1.64 kg
Total	β_1	66.4 kg/m^2
	β_2	302.0 kg/m^2
	Mass	2.82 kg
	Length	25.15 cm
	Outer radius	25 cm

Fig. 5 shows an overview of the nominal flight system, with a mass summary provided in Table 3 (including current best estimates (CBE), contingency, and maximum expected values (MEV)). It was found that a flight system consisting primarily of commercially available, off-the-shelf components can be feasibly constructed at a university scale, with a minimal budget when compared to more complex demonstrations. The total hosted mass of the spacecraft with contingency added is 24.9 kg, which falls well within the range of secondary payload requirements. Ref. 18 discusses the flight system in more depth.
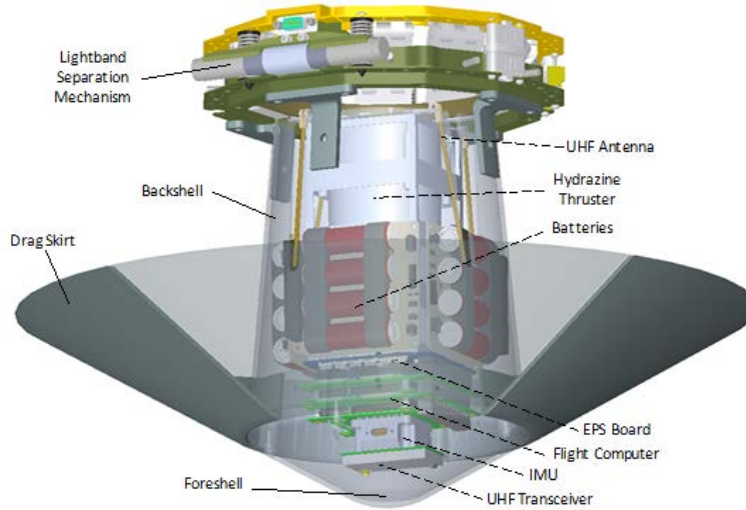

Figure 5. Key flight system components.

Table 3. Flight system mass summary.

Mass Summary	CBE	Contingency	MEV
	kg	%	kg
Flight System	**15.4**	**21%**	**18.7**
Spacecraft Bus	**7.8**	**12%**	**8.8**
Power	1.2	30%	1.6
C&DH	0.2	30%	0.2
Telecom	0.1	14%	0.1
Structure	0.7	30%	0.9
Thermal	4.2	0%	4.2
Propulsion	0.6	30%	0.8
GN&C	0.1	5%	0.1
Cabling	0.7	15%	0.8
Aeroshell	**7.6**	**30%**	**9.9**
Margin			**18%**
JPL Mass Margin			30%
JPL Margined Dry Mass			**22.1**
Total Propellant			**0.74**
Propellant			0.74
Spacecraft-side Separation System			0.51
Spacecraft Mass - Fully Margined			**23.3**
ComSat-side Separation System			1.62
Total Hosted Mass			**24.9**

III. Trajectory and Guidance Analysis

A. Trajectory Modeling

The smallsat will experience its most extreme conditions during the atmospheric portion of its trajectory. A numeric trajectory simulation was used to analyze the vehicle's performance during this phase. This simulation uses a fourth-order Runge-Kutta scheme to numerically integrate the 3-DOF equations of motion. The Earth was modeled as a sphere with inverse square gravity and J2 perturbations. Heating at the stagnation point was approximated using the Sutton-Graves relation, and radiative heating was not modeled. Nominal planetary atmospheres were formulated as a table look-up of different atmospheric properties as a function of altitude; these properties were generated via the Global Reference Atmospheric Model (GRAM) software for each planetary body[20]. Use of this simulation enabled quick analysis of peak deceleration, convective heat rates, and post-aerocapture orbits for potential trajectories.

Initial conditions for this simulation consist of the vehicle's state at atmospheric interface. This state for the spacecraft's nominal trajectory is shown in Table 4.

Table 4.   Trajectory simulation initial conditions.

Parameter	Value
Inertial velocity magnitude	10.3 km/s
Inertial flight path angle	-5.04°
Inertial azimuth	90°
Altitude	125 km
Latitude	0°
Longitude	169°

B. Guidance Algorithm Selection

In order to target the desired post-aerocapture orbit, the drag skirt jettison event must be controlled through the use of an appropriate guidance algorithm. Two different algorithms were considered for the purposes of this study: a low-fidelity deceleration curve-fit (DCF) method, and a high-fidelity numeric predictor-corrector (NPC) algorithm.

1. Deceleration Curve-Fit

The original implementation of the DCF algorithm under consideration for this study can be seen in Ref. 21, which describes the navigation processes used for Mars Pathfinder. As adapted to single-event-jettison aerocapture, the algorithm's structure is very similar. During atmospheric entry, the algorithm remains in standby until an initial deceleration value, g_1, is measured by the onboard accelerometers. After this measurement occurs, a timer is initiated. Once ΔT seconds have passed, a second deceleration measurement, g_2, is taken. This g_2 value is then compared against a pre-generated curve that maps g_2 measurements against time until jettison, t_{go}. The resulting t_{go} value is then used to schedule the jettison event.

As an example, the curve generated for Earth aerocapture in this study is shown in Fig. 6, in the form of a best-fit 3rd degree polynomial that interpolates discrete g_2 and t_{go} pairings. The trajectories used to generate these pairings are configured such that jettison is guaranteed to occur at a time which minimizes errors in final apoapsis altitude. For this study, a simulated annealing optimization approach was used to obtain the ideal jettison times for 20 different curve-fit trajectories over a diverse range of entry flight path angles.
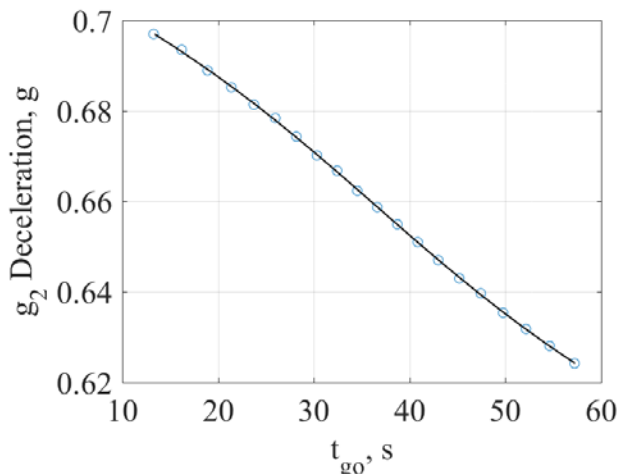

Figure 6. Jettison t_{go} curve fit for Earth aerocapture.

Table 5. Deceleration curve fit parameters

Configuration	Parameter	Value
Single-event-jettison aerocapture	g_1	0.3 g's
	ΔT	10 s
Mars Pathfinder parachute timing	g_1	5 g's
	ΔT	12 s

Table 5 shows the configuration of the algorithm parameters used for aerocapture guidance in this study, alongside the configuration used by Mars Pathfinder. Although the low g_1 value specified can increase the likelihood of false or pre-emptive triggers in a real flight situation, it is necessary to account for the potential of inbound aerocapture trajectories with steeper-than-expected entry flight-path angles, which require the jettison event to occur very early in atmospheric flight. The risks associated with this requirement can be mitigated by reducing uncertainty in entry state (enabling a higher g_1 value), or by taking a time-average of deceleration instead of an instantaneous measurement.

2. Numeric Predictor-Corrector

The NPC algorithm used for this study is described in detail in Ref. 9. The predictor phase of the algorithm uses accelerometer measurements to numerically propagate the spacecraft's current trajectory, in order to determine its state at atmospheric exit. The corrector uses this state to calculate the vehicle's post-aerocapture orbit and then adjusts the timing of the drag skirt jettison event accordingly, with the goal of minimizing error in final apoapsis altitude. The NPC also features a constant-bias atmospheric density correction factor to improve accuracy in the face of atmospheric uncertainties.

3. Comparison and Results

Monte Carlo simulations were run to examine the response of each guidance option to uncertainty. The specific dispersions applied are listed in Table 6. The entry flight-path angle variation was based on a preliminary uncertainty analysis on spacecraft's trajectory following the PLM. Atmospheric density and wind dispersions were generated by the Earth-GRAM atmospheric model[11].

Table 6. Guidance algorithm Monte Carlo dispersions.

Planetary Body	Parameter	Dispersion
Earth	Entry flight-path angle	0.12°
	Hypersonic C_A	3%
	Hypersonic C_N	5%
	Atmospheric density & wind variations	Earth-GRAM

Results from the Monte Carlo analyses are listed in Table 7. 5,000 samples were run for each guidance algorithm, with the NPC run twice: once at a low guidance rate, and once at a medium guidance rate. Each sample targeted a final apogee altitude of 1,760 km. The statistics for post-maneuver apoapsis altitude were determined only from the successful cases – cases that involve surface impact or failure to capture into orbit were excluded.

The DCF guidance algorithm was the least computationally intensive option, despite the high guidance rate chosen. This rate matched the spacecraft data acquisition rate to ensure accurate instantaneous deceleration measurements are achieved. Despite this, the curve-fit method performs quite poorly, with several cases that either fail to escape the atmosphere or fail to capture into orbit. Even amongst the successful cases, there is a large degree of variation from the target.

During data post-processing, it was determined that atmospheric density variations were by far the leading cause of failure for the DCF method. Although the algorithm is somewhat robust to uncertainties in entry state and spacecraft aerodynamics, changes in atmospheric density profile lead to correlations between g_2 and t_{go} that are different than those expected for a nominal atmosphere. Atmospheric variations were less of a concern for the original implementation of this algorithm on Mars Pathfinder, because the mission was less sensitive to its parachute deployment time; excess velocity accrued could later be zeroed out (to an extent) by the propulsive maneuver that was performed prior to landing. For the purposes of single-event-jettison aerocapture missions, some means of accounting for these atmospheric uncertainties is most likely required for this DCF method to be a viable guidance choice.

At both low and medium guidance rates, the NPC algorithm was more effective at targeting the desired final orbit. For both rates, every case was successful at capturing into orbit. Both the low and mid-rate choices resulted in mean apogee altitudes that were biased slightly below target, which indicates that the algorithm has a tendency to produce later-than-optimal jettison times. This is a byproduct of how the jettison event is scheduled within the NPC: jettison is only triggered when the predicted jettison time has been passed. This can result in slight delays in jettison timing, which can decrease the final apogee altitude by tens of kilometers due to the vehicle's sensitivity to this event. Histograms of the NPC results, displayed in Figure 7, show that this tendency is more pronounced for the low-rate selection, which exhibits a slightly bimodal distribution because of these late jettisons. This shape is not present in results for the mid-rate group, which produces more accurate final orbits with less variation (albeit at the cost of increased computation time).

Table 7.   5000-sample Monte Carlo simulation results.

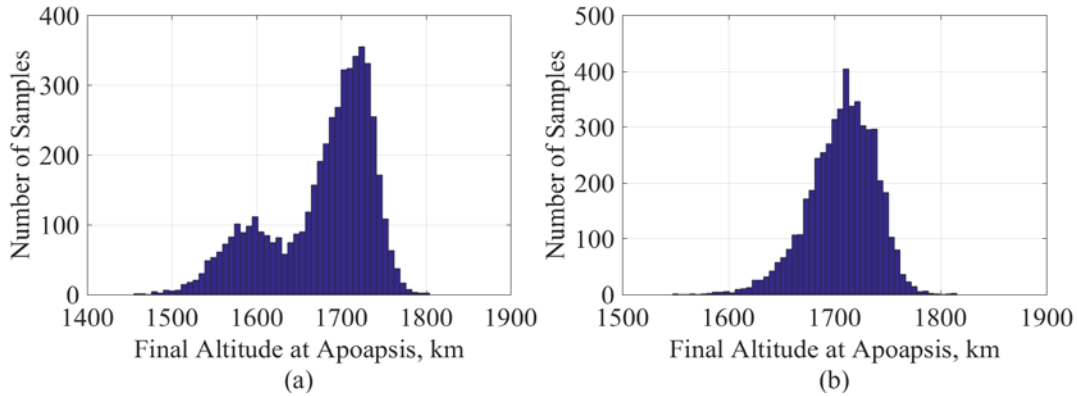| Parameter	Value		
Guidance scheme	DCF	Low-rate NPC	Mid-rate NPC
Guidance execution rate	50 Hz	1 Hz	5 Hz
Mean computation time	0.20 s	0.30 s	0.60 s
Number of surface impacts	1729	0	0
Number of escape trajectories	0	0	0
Mean apogee altitude	4441.8 km	1677.2 km	1707.2 km
3σ apogee altitude deviation	2532.2 km	60.7 km	31.3 km
Apogee altitude range	11656.9 km	349.5 km	268.2 km

Figure 7. NPC Monte Carlo histograms: (a) 1 Hz, and (b) 5 Hz.

Based on this analysis (detailed further in Ref. 19), a low-rate NPC was selected as the nominal guidance algorithm for this mission. For the purposes of an initial demonstration, the accuracy offered by the low-rate option is likely sufficient. The reduction in computational cost is also significant, considering the throughput of the smallsat-scale flight computers that may be used. For missions with greater accuracy requirements, it may be necessary to run this guidance algorithm at a higher rate, or consider different drag modulation control schemes (such as a multi-stage jettison approach.)

C. Nominal Trajectory Results

Figure 8 shows the key simulation results for the spacecraft's nominal trajectory. During atmospheric flight, the vehicle reaches a minimum altitude of approximately 70 km. Once the flight computer determines enough energy has been lost, the external drag skirt is jettisoned. As a result, an instantaneous increase in β occurs and less atmospheric drag is experienced by the vehicle. This produces the discontinuity seen in the deceleration plot.
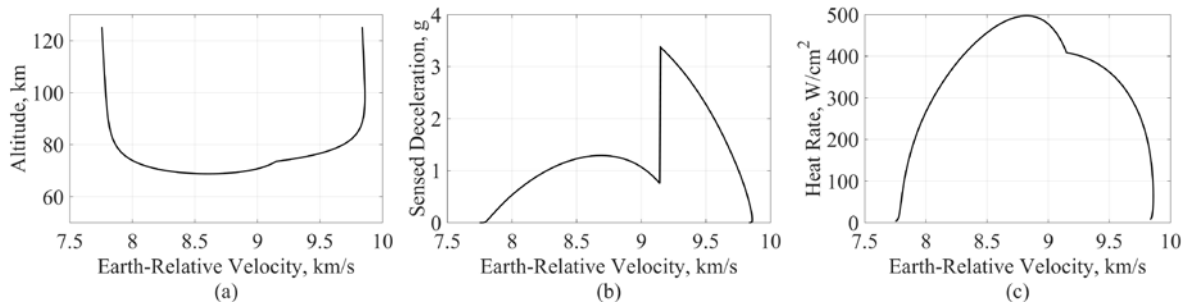
Figure 8. Nominal aerocapture trajectory: (a) altitude, (b) sensed deceleration, and (c) stagnation point heat rate versus Earth-relative velocity.

IV. Uncertainty Analysis

An end-to-end Monte Carlo analysis was run to examine the robustness of the proposed mission and spacecraft design to uncertainty. This analysis considered sources of error throughout the spacecraft's entire trajectory to determine potential variation from the desired final orbit. Uncertainties were introduced at three distinct points: the PLM, the atmospheric portion of the aerocapture maneuver, and the PRM. The uncertainty sources considered and their values are shown in Table 8.

Table 8. End-to-end Monte Carlo simulation uncertainty sources.

Trajectory Phase	Parameter	Dispersion
Perigee-lower maneuver	Initial GTO perigee	± 2 km
	Initial GTO apogee	± 10 km
	Coast time	± 300 s
	Burn ΔV	± 1.17%
Atmospheric flight	Atmospheric density & wind variations	Earth-GRAM
Perigee-raise maneuver	Coast time	± 300 s
	Burn ΔV	± 1.06%

The state errors from each distinct trajectory phase were propagated forward and considered as a source of error for subsequent phases. PLM and PRM coast times are a measurement of time until each burn is performed, from rideshare separation and atmospheric exit respectively. Burn ΔV dispersions were determined from manufacturer specifications for the proposed propulsion system, using IMU measurements as a cutoff value. Atmospheric uncertainties were obtained using Earth-GRAM 2010. The PLM burn magnitude is the driving source of uncertainty for this end-to-end simulation, as small variations can have a large effect on the flight path angle at atmospheric interface.

Table 9 shows the results of this Monte Carlo simulation. 10,000 samples were run, with a target final apogee altitude of 1,760 km and final perigee altitude of 180 km. The mean apogee and perigee are close to the desired values, signifying that the desired final orbit can be targeted with a reasonable degree of accuracy. Histogram plots of the results are shown in Fig. 9. Much like the NPC results discussed in Table 7 and Figure 7, the apogee altitudes shown here are biased slightly below the target 1760 km. As modeled, the final apogee has a range of 210.2 km, while the final perigee range is 14.2 km. This level of

Table 9. End-to-end Monte Carlo simulation results.

Apsis	Parameter	Value
Apogee	Mean	1693.7 km
	3σ	169.5 km
	Minimum	1556.5 km
	Maximum	1766.7 km
Perigee	Mean	180.3 km
	3σ	4.8 km
	Minimum	174.1 km
	Maximum	188.3 km

accuracy is suitable for the purposes of this flight demonstration, although further precision would likely be required for future missions with more significant targeting requirements.
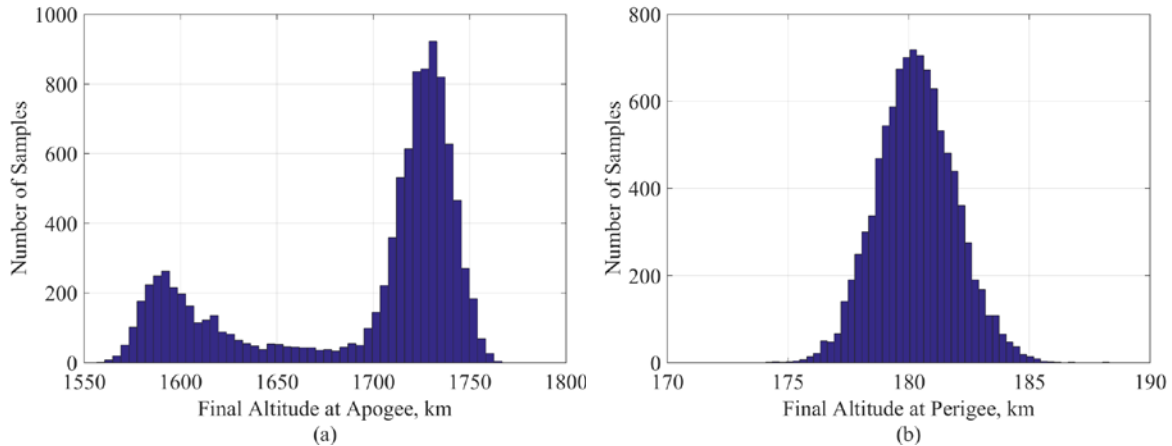
Figure 9. End-to-end Monte Carlo histograms: (a) final altitude at apogee, and (b) final altitude at perigee.

V. Relevance to Mars

A flight demonstration of aerocapture should have relevance to desired applications of the technique at different planetary targets. To this end, analogues can be drawn from the proposed Earth demonstration to orbital insertion at Mars, as the 2 km/s ΔV requirement is similar to that required for capture into a low Mars orbit. To assess the relevance of this mission concept to Martian aerocapture, trajectory and uncertainty analyses were carried out for an identical vehicle using single-event drag modulation to capture into orbit at Mars. For the purpose of these simulations, it is assumed that the smallsat is initially flying an eastbound equatorial trajectory, with initial conditions at atmospheric interface given in Table 10. The target orbit is identical to that of the Earth demonstration, with an apoapsis altitude of 1,760 km and a periapsis altitude of 180 km. Trajectory simulation results for nominal flight are shown in Fig. 10. Both the convective heat rate and peak deceleration are lower than those experienced during the proposed Earth flight test; therefore, a successful flight demonstration will validate an aerocapture system for environments more rigorous than what may be necessary for actual missions.

Table 10. Mars trajectory simulation initial conditions.

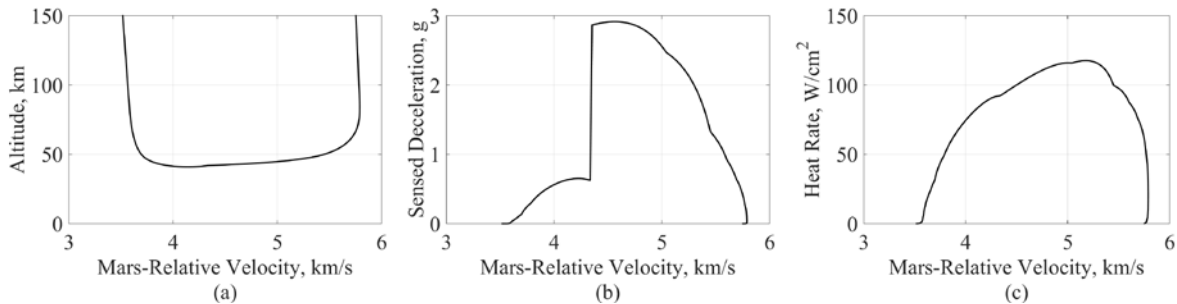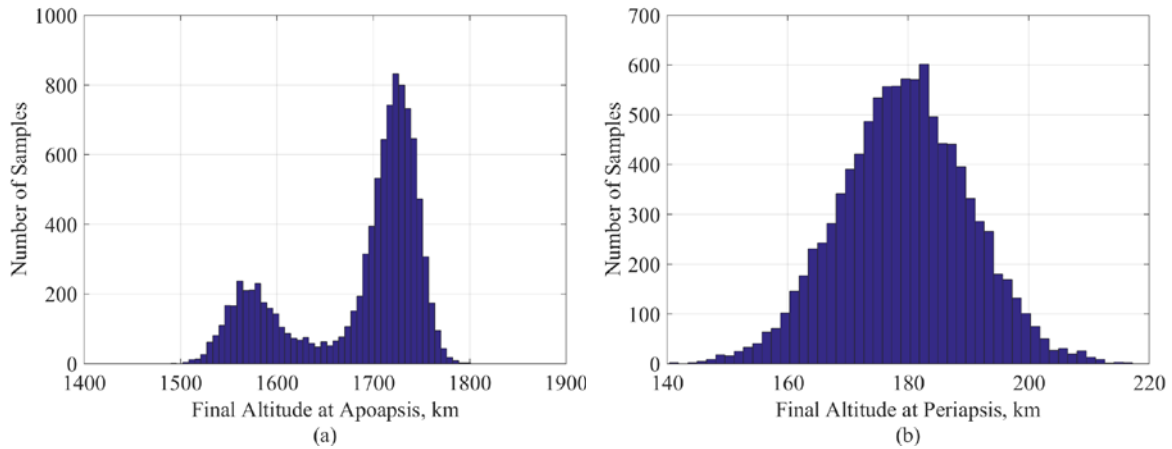| Parameter	Value
Inertial velocity magnitude	6.0 km/s
Inertial flight path angle	-12°
Inertial azimuth	90°
Altitude	150 km
Latitude	0°
Longitude	0°

Figure 10. Nominal Mars aerocapture trajectory: (a) altitude, (b) sensed deceleration, and (c) stagnation point heat rate versus Mars-relative velocity.

To assess uncertainty, a similar end-to-end Monte Carlo analysis was performed, featuring errors introduced at atmospheric interface and the subsequent PRM. State errors at atmospheric interface are based on MSL approach navigation results[12], and errors during the PRM were generated similarly to those for the Earth demonstration. These dispersions are listed in Table 11.

Table 11. Mars end-to-end Monte Carlo simulation uncertainty sources.

Trajectory Phase	Parameter	Dispersion
Atmospheric interface & flight	Entry flight path angle	± 0.013°
	Atmospheric density & wind variations	Mars-GRAM
Perigee-raise maneuver	Coast time	± 300 s
	Burn ΔV	± 1.08%

Results for a 10,000 sample Monte Carlo are shown in Table 12 and Fig. 11. Similar to the results from the Earth simulations, the apoapsis histogram displays a bimodal distribution that is biased slightly below the target. The apoapsis and periapsis ranges indicate that the spacecraft is able to capture into Mars orbit successfully, with some variation. Although greater precision is likely required for Mars science missions, an actual Mars aerocapture vehicle will be far less limited by rideshare constraints than the one considered in this research. Realistically, such a vehicle could feature a much larger change in β during drag modulation, which could lead to a more accurate final orbit.

Figure 11.   Mars end-to-end Monte Carlo histograms: (a) final altitude at apoapsis, and (b) final altitude at periapsis.

Table 12. Mars end-to-end Monte Carlo simulation results.

Apsis	Parameter	Value
Apoapsis	Mean	1685.0 km
	3σ	201.3 km
	Minimum	1490.0 km
	Maximum	1801.0 km
Periapsis	Mean	179.4 km
	3σ	32.5 km
	Minimum	140.4 km
	Maximum	217.2 km

VI.   Conclusion

A comprehensive mission concept for an Earth-based flight demonstration of drag-modulated aerocapture has been developed. The proposed concept would help to validate the use of aerocapture, provide data products from the maneuver, and has relevance to missions at Mars and other targets. Trajectory and uncertainty analyses show the feasibility of the proposed trajectory. Monte Carlo analyses also demonstrate the robustness of the selected low-rate numeric predictor-corrector guidance algorithm to day-of-flight uncertainties. Mechanical and systems evaluations show that a 24.9 kg spacecraft featuring commercially-available components can survive the rigors of an aerocapture maneuver.

Future developmental work for this mission concept may include development of a mechanism to enable spinning separation from the host spacecraft, further investigation into the static and dynamic stability characteristics of the vehicle, higher-fidelity analysis of the drag skirt jettison event and further exploration of the guidance algorithm trade space. In-depth modeling of the drag skirt jettison event can help minimize the risks of recontact. Further guidance algorithm development may yield improvements to the deceleration curve-fit algorithm, which may make it worth revisiting as the least computationally-intensive option.

Acknowledgments

References

[1]Walberg, G. D., "A Survey of Aeroassisted Orbit Transfer," *Journal of Spacecraft and Rockets*, Vol. 22, No. 1, 1985, pp. 3-18.

[2]Hall, J. L., Noca, M. A., and Bailey, R. W., "Cost-Benefit Analysis of the Aerocapture Mission Set," *Journal of Spacecraft and Rockets*, Vol. 42, No. 2, 2005, pp. 309-320.

[3]Miller, K. L., Gulick, D., Lewis, J., Trochman, B., Stein, J., Lyons, D. T., and Wilmoth, R. G., "Trailing Ballute Aerocapture: Concept and Feasibility Assessment," *39th AIAA/ASME/SAE/ASEE Joint Propulsion Conference and Exhibit*, Huntsville, AL, July 2003.

[4]Lockwood, M. K., "Titan Aerocapture Systems Analysis," *39th AIAA/ASME/SAE/ASEE Joint Propulsion Conference and Exhibit,* Huntsville, AL, July 2003.

[5]Lockwood, M. K., "Neptune Aerocapture Systems Analysis," *AIAA Atmospheric Flight Mechanics Conference and Exhibit*, Providence, RI, August 2004.

[6]Hall, J. L., "An Overview of the ST-7 Aerocapture Flight Test Experiment," *AIAA Atmospheric Flight Mechanics Conference and Exhibit*, Monterey, CA, August 2002.

[7]McRonald, A., "A Light-Weight Inflatable Hypersonic Drag Device for Planetary Entry," *Association Aeronautique de France Conference*, Arcachon, France, March 1999.

[8]Lyons, D. T., and Johnson, W. R., "Ballute Aerocapture Trajectories at Neptune," *AIAA Atmospheric Flight Mechanics Conference and Exhibit*, Providence, RI, August 2004.

[9]Putnam, Z. R., Clark, I. G., and Braun, R. D., "Drag Modulation Flight Control for Aerocapture," *Aerospace Conference, 2012 IEEE*, Big Sky, MT, March 2012, pp. 1-10.

[10]Putnam, Z. R., and Braun, R. D., "Drag Modulation Flight Control System Options for Planetary Aerocapture," *Journal of Spacecraft and Rockets*, Vol. 51, No. 1, 2014, pp. 139-150.

[11]Leslie, F. W., and Justus, C. G., "The NASA Marshall Space Flight Center Earth Global Reference Atmospheric Model-2010 Version," NASA/TM-2011-216467, June 2011.

[12]Martin-Mur, T. J., Kruizinga, G. L., and Wong, M. C., "Mars Science Laboratory Interplanetary Navigation Analysis," *22nd International Symposium on Space Flight Dynamics*, São José dos Campos, Brazil, March 2011.

[13]Mitcheltree, R. A., Moss, J. N., Cheatwood, F. M., Greene, F. A., and Braun, R. D., "Aerodynamics of the Mars Microprobe Entry Vehicles," *Journal of Spacecraft and Rockets*, Vol. 36, No. 3, 1999, pp. 392-398.

[14]Cheatwood, F. M., Merski, N. R., Jr., Riley, C. J., and Mitcheltree, R. A., "Aerothermodynamic Environment Definition for the Genesis Sample Return Capsule," *35th AIAA Thermophysics Conference*, Anaheim, CA, June 2001.

[15]Mitcheltree, R. A., Wilmoth, R. G., Cheatwood, F. M., Brauckmann, G. J., and Greene, F. A., "Aerodynamics of Stardust Sample Return Capsule," *Journal of Spacecraft and Rockets*, Vol. 36, No. 3, 1999, pp. 429-435.

[16]Kinney, D. J., "Aero-Thermodynamics for Conceptual Design," *42nd AIAA Aerospace Sciences Meeting and Exhibit*, Reno, NV, January 2004.

[17]Woollard, B. A., and Braun, R. D., "Mechanical Design of a Cubesat Aeroshell for an Earth Demonstration of Single-Stage Drag Modulated Aerocapture," SSDL Masters Projects, Georgia Institute of Technology, Atlanta, GA, 2016 (unpublished).

[18]Werner, M. S., et al., "Development of an Earth Smallsat Flight Test to Demonstrate Viability of Mars Aerocapture," *55th AIAA Aerospace Sciences Meeting*, Grapevine, TX, January 2017.

[19]Werner, M. S., and Braun, R. D., "Characterization of Guidance Algorithm Performance for Drag Modulation-Based Aerocapture," AAS 17-032, 2017 AAS Guidance, Navigation and Control Conference, Breckenridge, CO, February 2017.

[20]Duvall, A. L., Justus, C. G., and Keller, V. W., "Global Reference Atmospheric Model (GRAM) Series for Aeroassist Applications," *43rd AIAA Aerospace Sciences Meeting and Exhibit*, Reno, NV, Jan. 2005.

[21]Braun, R. D., Spencer, D. A., Kallemeyn, P. H., and Vaughan, R. M, "Mars Pathfinder Atmospheric Entry Navigation Operations", *22nd Atmospheric Flight Mechanics Conference*, New Orleans, LA, August 1997.